Volume 1 | Number 1 | Jan 2013 | Pages 1–100

Journal of
Materials Chemistry A

Materials for energy and sustainability
www.rsc.org/materialsA

Li⁺

ROYAL SOCIETY
OF CHEMISTRY

ROYAL SOCIETY
OF CHEMISTRY

www.rsc.org/materialsA

The pH-responsive smart nanocontainers based on the hollow mesoporous zirconia nanospheres are used to construct intelligent anticorrosion coatings.

ARTICLE TYPE

An Intelligent Anticorrosion Coating Based on pH-Responsive Smart Nanocontainers Fabricated via a Facile Method for Protection of Carbon Steel

MingDong Wang, MengYang Liu, and JiaJun Fu*[a]

Morphologically intact hollow mesoporous zirconia nanospheres (HMZSs) with a hollow core mesoporous shell structure were successfully synthesized by sol-gel protection method and used as scaffolds for smart nanocontainers. L-Carnosine (L-CAR) was proved as green, efficient and mixed-type
10 corrosion inhibitor for protection of carbon steel. Crucially, the net charge on L-CAR molecules is influenced by solution pH and matches the changing regularity of zeta potential of HMZSs. Taking advantage of the pH-dependent electrostatic interactions between HMZSs and L-CAR, the smart nanocontainers constructed by directly binding L-CAR to HMZSs easily achieve acid/alkaline-responsive controlled release. The smart nanocontainers, L-CAR loaded HMZSs were incorporated into water-borne
15 epoxy coating to assemble the intelligent anticorrosion coatings (IACs). The anticorrosion performances of IACs on carbon steel surface were systematically evaluated by electrochemical impedance spectroscopy and scanning vibrating electrode technique. Compared with the pure epoxy coating, IACs demonstrate the more excellent corrosion resistance ability. Through monitoring the corrosion around artificial scratches, it is observed that IACs display the satisfactory self-healing effects, which are
20 attributed to the fact that the smart nanocontainers respond spontaneously to local acidification in micro-anodic zones as well as local alkalization in micro-cathodic zones, subsequently release L-CAR molecules to compensate damaged coatings.

Introduction

The category of intelligent anticorrosion coatings (IACs) is an
25 important branch of modern smart coatings, which mimics the "injury-healing" principle of organisms and is capable of showing the self-diagnosis and self-healing functions against internal or external damage, eliminating potential hazard and extending service life of protected materials.[1-3] The unique
30 structure of "passive hosts and active guests" is now generally acceptable and regarded as the most promising candidate of IACs for industrialization.[4,5] The passive barrier coatings as primary components prevent aggressive species from reaching the surface of underlying substrates. The active guests as key components
35 carry the main tasks of detecting defects and self-healing automatically. According to the different working mechanisms and releasing triggers of active materials, IACs can be divided into two groups: (ⅰ) polymer healable materials (e.g., dicyclopentadiene, isocyanate, diglycidyl ether, bisphenol A/ethyl
40 phenylacetate, etc.).[6-11] Microcapsules, hollow fibers or microvascular networks containing polymer healable materials are introduced into polymer coatings, once polymer coatings are mechanically damaged, reactive chemicals will spill from damaged area and generate the internal glue by a variety of
45 chemical reactions, thus filling the microcracks partially or completely and restoring the original properties;[12,13] (ⅱ) corrosion inhibitors (e.g., cerium (Ⅲ) nitrate, 1H-benzotriazole, 8-hydroxyquinoline, 2-mercaptobenzothiazole, etc.).[14-16] The corrosion inhibitors are encapsulated into smart nanocontainers,
50 most often employing porous inorganic nanoparticles as scaffolds (e.g., mesoporous SiO_2, TiO_2, CeO_2, layered double hydroxide, halloysite nanotubes etc.). Smart nanocontainers can quickly respond to the changes of environmental factors arising from local corrosion processes and immediately release corrosion
55 inhibitors, forming protective molecular film on the corroded metal surface by chemisorption or physisorption processes to inhibit the corrosion expansion.[17-21] The utilization of the special coating structure can effectively protect metallic materials, including: aluminium, magnesium, steel, *etc*.

60 The research groups of Schukin and Zheludkevich have done much work covering the smart nanocontainers-based IACs and proposed many templates.[22-24] To better execute "intelligent" functions, stimuli-responsive shells are decorated on the outside of scaffolds by various chemical means, including polyelectrolyte
65 layer-by-layer assembly,[25] supramolecular assembly,[26,27] surface-grafted precipitation polymerization,[28] and terminal packaging etc.[29,30] But in general, most of the installation techniques are still at experimental stage due to their complex and cumbersome assembly. To simplify manufacturing processes, some researchers

have not designed gatekeepers for smart nanocontainers consciously.[31,32] However, the undesired leaching of corrosion inhibitors occurring in preparation or in normal state of IACs undermines anticorrosion performances.

Recently, Zheng et al. reported hollow mesoporous zirconia nanoparticles as drug delivery vehicles, which showed the surprising pH-stimuli responsive controlled release of drugs without any outside modification.[33] As proved previously, when carbon steel suffers from the attack of aggressive ion species (e.g. chloride or sulfate), the dissolution of ferrum and subsequent hydrolysis of ferrous or ferric ions lead to the decrease of pH values in the micro-anodic zones, while in the micro-cathodic zones, the oxygen reduction reaction results in the increase of pH values. Therefore, the fluctuations of pH values as typical features around corrosive microzones are usually served as triggers for releasing corrosion inhibitors.[28,29,34] In the present work, inspired by the work of Zheng et al., to begin with, morphologically intact and controllable hollow mesoporous zirconia nanospheres (HMZSs) were synthesized for the first time by sol-gel protection method as scaffolds for smart nanocontainers. Following this, with the precondition of green, efficient and easily available, the appropriate corrosion inhibitor was hand-picked for matching HMZSs and meets the demands as following: under neutral solution, the selected corrosion inhibitor is loaded in the hollow cavity of HMZSs by means of electrostatic attractions, but the corrosion inhibitor can be escaped easily in acidic or alkaline environment due to the gradually diminishing electrostatic attraction or generated electrostatic repulsion. The smart nanocontainers prepared by one-step loading process not only enhance the adsorption capacity relying on the hollow structure, but maintain acid/alkaline-responsive controlled release without building complex gatekeepers. Finally, the exquisitely designed smart nanocontainers were uniformly incorporated into water-borne epoxy coatings to construct IACs, which were subsequently deposited on carbon steel surface. The comprehensive anticorrosion performances and intelligent self-healing property were completely assessed.

Results and Discussion

Preparation of HMZSs Using Sol-Gel Protection Method

The preparation of HMZSs has been reported previously.[33,35] However, many repeated experiments in our laboratory verify that high temperature calcination, which facilitates crystallization of amorphous zirconia will cause disastrous damage to mesoporous shells, especially for HMZSs with thin shells. With the increase of calcination temperature, the problem became more and more serious (Fig. S1, Electronic Supplementary Information (ESI†)). Also, Yin et al. observed the same problem of shell collapse during the synthesization of hollow mesoporous anatase titania.[36] The broken HMZSs are attributed to the fact that interior stresses increase rapidly and shells are forced to rearrange during the grain growth process. But apparently, it is important to maintain the intact morphology of HMZSs, which are applied as scaffolds for pH-controlled release. The fragmentary hollow nanospheres cannot perform loading and controlled release tasks well. To overcome this problem, the sol-gel protection method was used to synthesize HMZSs for the first time and the key step is a thin silica layer formed on the exterior surface protects mesoporous zirconia shell in the course of calcination. The whole procedure is depicted in Fig. S2 (ESI†) and can be differentiated into four steps as follows: (ⅰ) preparation of monodispersed silica nanoparticles with expected diameter as hard templates by
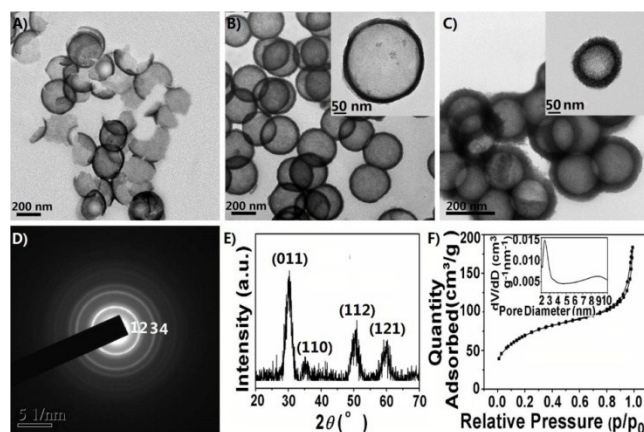
Fig. 1 TEM images of A) HMZSs synthesized without sol-gel layer protection; B) HMZSs-*d*300 synthesized under sol-gel layer protection; C) HMZSs-*d*150 synthesized under sol-gel layer protection; D) SAED pattern of HMZSs-*d*300; E) Powder XRD pattern for HMZs-*d*300; and F) N_2 adsorption-desorption isotherm and pore-size distribution of HMZSs-*d*300.

classical Stöber method; (ⅱ) deposition of a zirconia layer with desired thickness to afford $sSiO_2@ZrO_2$ nanocomposites through sol-gel reaction of zirconium butoxide with polyoxyethylene lauryl ether (Brij 30) as structure-directing agent; (ⅲ) deposition of a thin SiO_2 layer to afford $sSiO_2@sZrO_2@sSiO_2$ and after calcination to obtain $sSiO_2@mZrO_2@sSiO_2$; (ⅳ) chemical etching to remove SiO_2 materials including hard templates and protective layers by NaOH solution to form $@mZrO_2$ (HMZSs). Following the synthetic steps, the internal diameter and shell thickness can be easily regulated by changing the relative amount of chemical reagents, and HMZSs-*d*300 (internal diameter of ca. 300 nm, shell thickness of ca. 15 nm) as well as HMZSs-*d*150 (internal diameter of ca. 150 nm, shell thickness of ca. 30 nm) were fabricated successfully as scaffolds. Fig. 1A shows the typical transmission electron microscopy (TEM) image of HMZSs synthesized without sol-gel layer protection. The majority of nanospheres are broken and the morphology is irregular. In contrast to Fig. 1A, the TEM images of HMZSs synthesized under sol-gel protection from Fig. 1B and 1C demonstrate the non-aggregated, uniform and intact hollow nanospheres with setting inner diameter as well as shell thickness. Fig. 1B represents the HMZSs-*d*300, while Fig. 1C illustrates the HMZSs-*d*150. The crystalline structures of HMZSs-*d*300 are confirmed by selected area electron diffraction pattern (SAED, Fig. 1D) and powder X-ray diffraction patterns (XRD, Fig. 1E). The d-spacings corresponding to the diffraction rings of the SAED pattern matches well with the tetragonal phases of zirconia data from JCPDS database (No. 50-1089). The four well-resolved peaks at 30.4º, 35.3º, 50.4º, and 60.2º are indexed to the (011), (110), (112) and (121) diffraction planes, respectively, indicating after calcination at 900 ℃ under sol-gel protection, amorphous ZrO_2 can successfully convert to tetragonal structure. The crystalline structure of HMZSs-*d*150 is similar to HMZSs-*d*300 (Fig. S3, ESI†). The N_2 adsorption-desorption isotherm of HMZSs-*d*300 shows type Ⅳ isotherms, indicating the existence of mesopores (Fig. 1F). A narrow peak appears centered at 2.51 nm in the Barrett-Joyner-Halenda (BJH) pore size distribution curves. In addition, the Brunauer-Emmett-Teller (BET) specific surface area and total pore volume of HMZSs-*d*300 are calculated to be 254 m^2 g^{-1} and 0.24 cm^3 g^{-1}, respectively. Detailed physicochemical parameters of HMZSs-*d*150 are summarized in Table S1 for comparison.

Assembling Smart Nanocontainers and pH-Responsive Controlled Release

According to the specific zeta potential *vs.* solution pH profile of HMZSs (see Fig. S4 and S5 in ESI†, isoelectric point=2.39) and taking the ultimate mission of acid/alkaline-responsive controlled release into account, the selecting criterions of corrosion inhibitor for assembling smart nanocontainers are very strict. Except for the prime inhibition performance requirements, the net charge on the chosen corrosion inhibitor should be controlled by solution pH and forms a good coordination with HMZSs. L-Carnosine (L-CAR), scientifically named β-alany-L-histidine, is a dipeptide of amino acids β-alanine and L-histidine and widely used in food additive and cosmetic industry. To our knowledge, there haven't been any reports on L-CAR employed as metallic corrosion inhibitor. However, the two main components, β-alanine and L-histidine as green chemicals have exhibited excellent corrosion inhibition performances.[37,38] Therefore, the inhibition performances of L-CAR in different conditions were tested. The theoretical and electrochemical experimental results all prove that L-CAR acts as high efficient, mixed-type corrosion inhibitors for carbon steel (see Fig. S6-S10 in ESI†).

Each L-CAR molecule has three ionized groups: the carboxylic group (pK_1=2.76), the nitrogens of the imidazole ring (pK_R=6.72), and the amino group of the β-alanine section (pK_2=9.32), and the isoelectric point is calculated as 8.02.[39] The transformation of molecular net charge is illustrated in Fig. S11 (ESI†). On the basis of the above analysis, it is not difficult to infer that L-CAR is a reasonable alternative. At pH 7.0, according to the isoelectric point, L-CAR molecules carry weak positive charges and will be adsorbed inside the interior cavity of HMZSs by electrostatic attractions. As pH increases, the deprotonation of amino group will compel negative charged L-CAR molecules to release from HMZSs due to the strong electrostatic repulsion under alkaline conditions. On the other hand, with rapid increase in zeta potential of HMZSs, the electrostatic attraction between L-CAR molecules and HMZSs gradually reduces in the pH range from 7.0 to 2.39, which is the most likely pH variation domain for corrosive micro-anodic zones.[40,41] Additionally, with the continuous accumulation of positive charges, L-CAR molecules cannot pack well inside the cavity of HMZSs due to the intermolecular electrostatic repulsion. Considering these two factors, it can be deduced that there also exist the electrostatic forces to push L-CAR molecules out of HMZSs in acidic circumstances.

Before performing release kinetic experiments, the maximum amount of adsorbed L-CAR were measured as 271.3 μg (L-CAR) · mg^{-1} (HMZSs-d300) and 226.5 μg (L-CAR) · mg^{-1} (HMZSs-d150) respectively, by determining the concentration of L-CAR in the supernatant after thoroughly sonicating. Considering the fixed ratio of inner diameter and shell thickness between the two types of shells, a mathematical calculation was carried out to compare the adsorption capacity and the results show that saturated adsorbed amount for HMZSs-d300 is almost five times as many as that of HMZSs-d150 (Scheme S1, ESI†). A large gap between ideal and realistic data reveals that some factors have an impact on loading efficiency, including L-CAR diffusion state, size of mesopores and L-CAR molecules, intermolecular repulsion between aggregated molecules and so on. The release kinetics of L-CAR loaded HMZSs-d300 and L-CAR loaded HMZSs-d150 under different pH values are shown in Fig. 2A. The clear pH-dependent release profiles are observed and the release rates are in the following order: alkaline > acidic
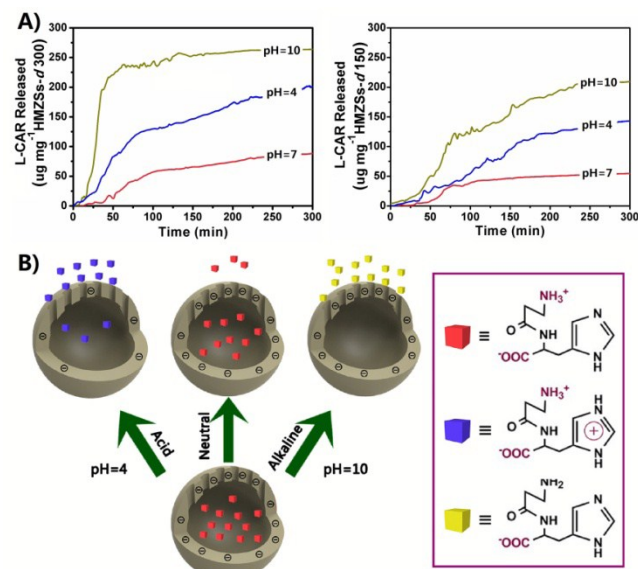

Fig. 2 A) Release profiles of L-CAR molecules from L-CAR loaded HMZSs-d300 and L-CAR loaded HMZSs-d150 under different pH value; and B) Schematic illustration of the releasing mechanism for L-CAR loaded HMZSs.

> neutral, as expected. These phenomena can be schematically explained by Fig. 2B which were discussed above. The premature release amounts of L-CAR molecules within 300 min under pH 7.0 approximately occupy 25% and 22% of total contents for L-CAR loaded HMZSs-d300 and L-CAR loaded HMZSs-d150, respectively. The electrostatic blocking strategy is less effective than supramolecular nanovalves or end stoppers,[26,27,30] in which the undesired release is near to zero, but, its level is close to those of multilayer-polyelectrolyte shells and far outstrips the other non-valves modes.[32,42] The premature release of L-CAR molecules maybe occur in the manufacture process of IACs. However, the remaining L-CAR molecules are relatively stable and enough to guarantee the self-healing effects. It is conceivable that the smart nanocontainers with simple structure, regulating the flow of L-CAR molecules upon pH changes are in urgent need. Compared with the other sophisticated gatekeepers, L-CAR loaded HMZSs manifest a good balance between performances and complexity of preparation. As transverse comparison, the release rate of HMZSs-d300 is faster than that of HMZS-d150 at the same condition. Under pH 10.0, even 90% of adsorbed L-CAR molecules are released from L-CAR loaded HMZSs-d300 only within 70 min. The thinner the mesoporous shell, the smaller the diffusion resistance, the faster release rate seems reasonable.

**Characterization and Anticorrosion Performance of IACs**

The commercial water-borne two component epoxy coating comprising Araldite PZ 3961 and Aradur 3985 was employed in this work as the passive coating to protect the underlying carbon steel specimens. The synthesized smart nanocontainers, L-CAR loaded HMZSs-d300 or L-CAR loaded HMZSs-d150 were well dispersed in the epoxy coatings and thus fabricating IACs-Ⅰ and IACs-Ⅱ by spin-coating method, respectively. The proportions of incorporated smart nanocontainers in IACs were all fixed as 1.5 wt%. The atomic force microscopy images of all the tested coatings shown in Fig. 3A demonstrate that the addition of the smart nanocontainers significantly increase coating surface roughness, from 2.4 nm to 13.8 nm (for IACs-Ⅰ) and 9.5 nm (for IACs-Ⅱ), respectively. The average thicknesses of IACs-Ⅰ and
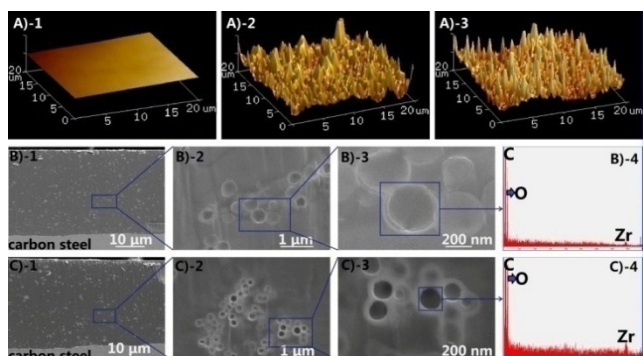
Fig. 3 A) AFM images of pure epoxy coating (A-1), IACs-Ⅰ (A-2), and IACs-Ⅱ (A-3); B) SEM images (including high-resolution SEM image) of the cross sectional views of the carbon steel specimen coated by IACs-Ⅰ containing L-CAR loaded HMZSs-*d*300 (B-1, B-2, and B-3) and EDX spectrum of the selected smart nanocontainer (B-4); and C) SEM images (including high-resolution SEM images) of the carbon steel specimen coated by IACs-Ⅱ containing L-CAR loaded HMZSs-*d*150 (C-1, C-2, and C-3) and EDX spectrum of the selected smart nanocontainer (C-4).

IACs-Ⅱ estimated from the cross-sectional scanning electron microscope images (CS-SEM, Fig. 3B-1 and 3C-1) are very similar and about 30 μm. Contrasting with the pure epoxy coating (the CS-SEM image is not shown here), the smart nanocontainers has little effects on the coating thickness. After being treated with plasma polishing machine (SM-09010, JEOL), the high-resolution CS-SEM images and the corresponding EDS images were obtained and illustrated in Fig. 3B and 3C-2~4. It can be easily observed that the incorporated smart nanocontainers are homogeneously distributed in the coatings and no large agglomerated nanocontainers are found, proving the high compatibility between the smart nanocontainers and components of aqueous epoxy coatings.

Electrochemical impedance spectroscopy (EIS) is a non-destructive measurement, which is employed to detect the electrochemical changes of a coated metal, quantify accurately by equivalent circuit method and thus make an evaluation of anticorrosion performances for coatings. The impedance behaviours for pure epoxy coating, IACs-Ⅰ and IACs-Ⅱ are presented in Bode (Fig. 4A) and Nyquist plots (Fig. 4B) as a function of immersion time. In the early stages of immersion, the total impedances of the three investigated coatings were almost identical. The coating capacitive behaviours extending over the whole frequency range in Bode plots and the large capacitive arcs in Nyquist plots indicate the excellent barrier properties. After being immersed for 10 days, the impedance diagrams of IACs-Ⅰ and IACs-Ⅱ were essentially the same as their original states, while the Nyquist plot of pure epoxy coating changed dramatically. The diameter of capacitive arc reduced remarkably at high frequency and the straight line corresponding to a diffusive Warburg behaviour in the low frequency range appeared which demonstrated that the gradually weakened anti-penetrating capability and the occurrence of diffusion controlled process within the pure epoxy coating. For the immersion test up to the 20th day, the Warburg impedance was replaced by another incomplete semicircle in the Nyquist plots and the resistive plateau appeared in the low frequency in the Bode plot, indicating that the corrosion process developed from diffusion control to charge transfer control at coating/metallic substrate interface and
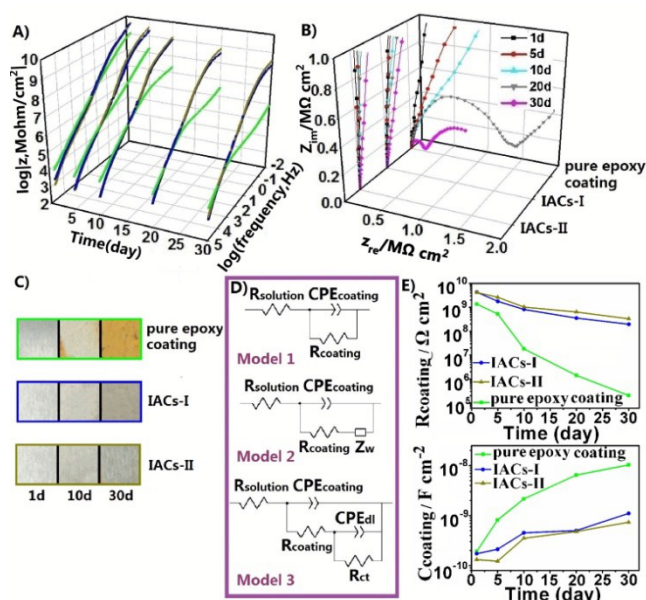
Fig. 4 A) Bode plots obtained on the carbon steel specimens coated with the pure epoxy coating (green), IACs-Ⅰ (blue), and IACs-Ⅱ (dark yellow) and B) Nyquist plots obtained on the carbon steel specimens coated with the pure epoxy coating, IACs-Ⅰ and IACs-Ⅱ after 1, 5, 10, 20, 30 days of immersion in 1.0 M NaCl; C) Optical photos of the carbon steel specimens coated with the pure epoxy coating, IACs-Ⅰ and IACs-Ⅱ taken with time elapse; D) The equivalent circuit models used to fit the EIS data; and E) Evolution of $R_{coating}$ and $C_{coating}$ by fitting EIS data using the appropriate equivalent circuits.

the undercoating corrosion started. Meanwhile, several pinholes and defects became distinct in the pure epoxy coating. In contrast, IACs-Ⅰ and IACs-Ⅱ all displayed the defect-free, homogeneous surface morphological structure (Fig. 4C), which were in consonance with the almost unchanged impedance profiles and corroborate their good protection against corrosion over a long period of time. After the end of the immersion tests on the 30th day, the pure epoxy coating was severely corroded and the corrosion products were clearly visible. The impedance values of IACs-Ⅰ and IACs-Ⅱ decreased one order of magnitude, however, the absence of the second time constant evidences the persistent barrier type of protection.

Impedance data were analyzed by the three different equivalent circuit models (Fig. 4D) to interpret the evolution process. Model 1 is used to simulate the simplistic one-time constant cases, in which constant phase element of the coating ($CPE_{coating}$) in parallel with the coating resistance ($R_{coating}$) is in series with the solution resistance ($R_{solution}$). In Model 2, the Warburg impedance (Z_W) is introduced and in series with $R_{coating}$ to account for the straight line observed at low frequency. Model 3, abbreviated as $R_{solution}(CPE_{coating}(R_{coating}(CPE_{dl}R_{ct})))$, in which R_{ct} and CPE_{dl} represent the charge transfer resistance and constant phase element for electric double layer, respectively, is applied for the two-time constants cases. In these three models, CPEs are used instead of pure capacitors due to surface heterogeneities. The capacitance values we focus on are given by $C=Y_0(\omega_{max})^{n-1}$, where Y_0 and n are parameter calculated for CPEs by using ZsimpWin 3.1 software and $\omega_{max}=2\pi f_{max}$, f_{max} is the frequency at which the imaginary component of the impedance is maximal.

The evolution of R$_{coating}$, measuring resistance to aggressive species transfer through the coating, and C$_{coating}$, reflecting water uptake tendency of coatings are shown in Fig. 4E. Coatings with high Rcoating values and low C$_{coating}$ values have been considered to offer good anticorrosion performance. During the entire immersion period, the decreasing trend of R$_{coating}$ (from 1.36×10^{9} to 2.02×10^{5} Ω cm^{2}) and the continuous increasing C$_{coating}$ values (from 1.91×10^{-10} to 4.31×10^{-8} F cm^{-2}) of pure epoxy coating indicate that the barrier is gradually deteriorated by water penetration. In comparison, the R$_{coating}$ and C$_{coating}$ values of two IACs remain relatively stable during 20 days of immersion. After that, small drop of R$_{coating}$ and slight rise in C$_{coating}$ are observed. These slight degradations do not influence the overall anticorrosion performance, which are proved by the optical photos taken after end of immersion (Fig. 4C). There is no doubt that L-CAR loaded HMZSs-*d*300 or L-CAR loaded HMZSs-*d*150 plays the critical role in prolonging anticorrosion effect. Their possible influences are mainly concentrated on the following two aspects: (ⅰ) the L-CAR loaded HMZSs-*d*300 and L-CAR loaded HMZSs-*d*150 have good compatibility with the epoxy coatings, the homogeneously dispersed smart nanocontainers efficiently fill the inherent pores and defects within coatings, decrease the porosity and delay the rate of invasion of water and chloride ions. (ⅱ) Once the diffusion pathways are formed and corrosion occurs, the smart nanocontainers, which are nearest or transfer to the damaged area release corrosion inhibitors to prevent spread of corrosion. By close comparison and analysis, the protective performance of IACs-Ⅱ incorporated with L-CAR loaded HMZSs-*d*150 is somewhat superior to that of IACs-Ⅰ containing L-CAR loaded HMZSs-*d*300, which is in agreement with the experimental results hold by Borisova *et al.*[43] Decreasing the size of nanocontainers to a certain extent will help to increase impermeability of the coatings.

Investigation of Self-Healing Functions

The preliminary assessments of self-healing properties of IACs were also obtained by EIS measurements, which were performed on the three coated carbon steel specimens with the crossed scratches of size 10 mm × 0.1 mm in 0.1 M NaCl solution. The artificial scratches were made carefully to avoid damaging the metal surface. $|Z|_{0.01Hz}$, the impedance modulus at a frequency of 0.01 Hz, which is always used to represent the corrosion resistance of the coatings is focused on.[31] In these cases, the higher $|Z|_{0.01Hz}$ value indicates the better self-healing for scratches. In the beginning, the Bode plots in Fig. 5A displayed two time constants, the resistive plateaus in low frequency reflect onset of corrosion process, which can be ascribed to the direct exposure of bared metal surface to corrosive medium. In the meantime, the $|Z|_{0.01Hz}$ values of pure epoxy coating, IACs-Ⅰ and IACs-Ⅱ were 0.158, 0.362, and 0.234 MΩ cm^{-2}, respectively. With increasing immersion time, the $|Z|_{0.01Hz}$ values of the three coatings all declined as shown in Fig. 5B, however, the downward trend of pure epoxy coating was much more obvious in comparison with IACs-Ⅰ and IACs-Ⅱ. Until the end of immersion, the $|Z|_{0.01Hz}$ value of IACs-Ⅰ was nearly two orders of magnitude higher than the one for the pure epoxy coating. The optical images of the scratched coating surface in different immersion period are shown in Fig. 5C. The corrosion along the crossed scratches on pure epoxy coating emerged right after immersion. As time went on, the corrosion became progressively worse. After 48 h immersion, the corroded area expanded greatly, the severe coating delamination was also observed. Through the whole immersion process, IACs-Ⅰ and IACs-Ⅱ showed less extension of corrosion along the scratches and remained good adhesion
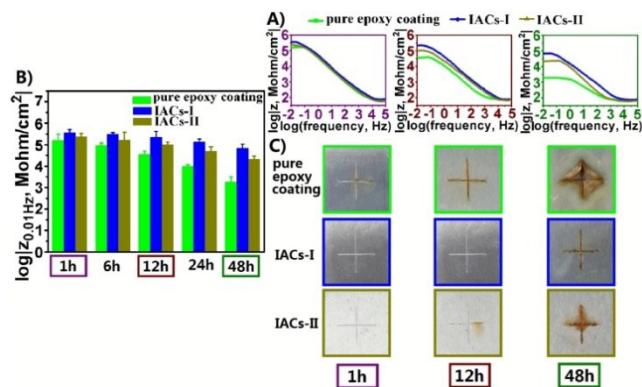

Fig. 5 A) Bode plots obtained on the coated carbon steel specimens with the artificial scratches after 1, 12 and 48 h immersion in 0.1 M NaCl; B) $|Z|_{0.01Hz}$ values of the coated carbon steel specimens with the artificial scratches at different immersion time; and C) Photographs of the evolution of corrosion behaviour occurring around the artificial scratches.

without any signs of delamination. The red rust accumulated at the scratched area for each IACs was much less than that for the pure epoxy coating. The changing trend of $|Z|_{0.01Hz}$ and the evolving optical images of the scratched surface prove that the protective effectiveness for scratches made by IACs-Ⅰ is better than IACs-Ⅱ. Undoubtedly, the inherent differences between two types of L-CAR loaded HMZSs account for the different manifestations in self-healing processes.

The Scanning Vibrating Electrode Technique (SVET) with superior sensitivity and high spatial resolution properties is used to investigate the localized corrosion process by measuring potential gradients originated from the oriented movement of ionic flux between the local anodic and cathodic sites and regarded as the powerful technique to quantify the self-healing ability of protective coating due to its nondestructive feature. The continuous SVET measurements of corrosion current densities in the vicinity of the scratched area were performed in 0.02 M NaCl, and the evolution processes of 3D current density maps for pure epoxy coating, IACs-Ⅰ and IACs-Ⅱ are presented in Fig. 6A-I, respectively. After 1 h immersion of pure epoxy coating, an initial well-defined anodic current peak associated with the iron dissolution was located around the scratched region. Some weak cathodic current peaks were also detected and distributed on the edge of scratches. At the same time, neither anodic nor cathodic current peaks were observed on the scanned area for the two IACs. With continued exposure of the pure epoxy coating, the anodic current area dramatically expanded and the current intensity became greater. The maximum anodic current density reached the value of 22.9 μA cm^{-2} after immersion of 24 h. By comparison, IACs demonstrate the protective ability and retard corrosion rate for the bared metal surface due to the presence of smart nanocontainers. During the whole immersion process, almost no cathodic current peak was found, and the anodic current densities located in the limited area after immersion for 24 h were 6.7 and 10.4 μA cm^{-2} for IACs-Ⅰ and IACs-Ⅱ, respectively, as presented in Fig. 6F and Fig. 6I, which were much smaller than that of the pure epoxy coating.

The observed self-healing phenomena of IACs and the incorporated smart nanocontainers are strongly coupled. One might speculate that the self-healing process of IACs makes up of four steps: (ⅰ) when the surface of carbon steel is intentionally scratched, the corrosive species can easily reach the metal surface and thus initiate corrosion; (ⅱ) under the neutral corrosive
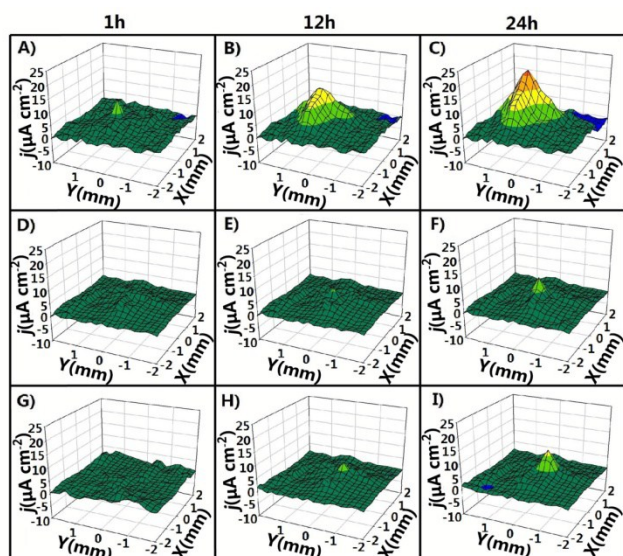
Fig. 6 SVET maps of the ionic currents measured above the scratched surface of carbon steel specimens coated with the pure epoxy coating (A, B, and C); with IACs-Ⅰ (D, E, and F); and
5 with IACs-Ⅱ (G, H, and I) at different time after immersion in 0.02 M NaCl.

environment, numerous micro-anodic zones and micro-cathodic zones are formed in the defected area. As the corrosion process continues, the micro-anodic zones appear to be local acidification
10 trend due to the hydrolysis of dissolved ferrous or ferric ions, while the micro-cathodic zones reveal local alkalization momentum ascribed to the oxygen reduction reaction; (ⅲ) the smart nanocontainers, such as L-CAR loaded HMZS-*d*300 or L-CAR loaded HMZS-*d*150 leave from the cracked coating and
15 gravitationally gather in the defected area, which make them experience the sudden changes of pH; (ⅳ) no matter in micro-anodic zones or in micro-cathodic zones, the entrapped L-CAR molecules, are quickly released from smart nanocontainers due to the acid/alkaline-responsive controlled release property. The free
20 mix-type L-CAR molecules are adsorbed on the exposed carbon steel surface and form molecular film to suppress both anodic and cathodic activities and compensate the damaged coating. In order to further verify the healing efficacy of L-CAR, the unloaded HMZSs-*d*300 were incorporated into the water-borne epoxy
25 coatings and the control experimental results of EIS and SVET were shown in Fig. S12 (ESI†). It was clear that with the increase of immersion, the anodic current peaks near the scratches climbed sharply (about 22.0 μA cm^{-2} after immersion for 24 h), and simultaneously $|Z|_{0.01Hz}$ values declined noticeably (from 0.234 to
30 0.0103 MΩ cm^{-2} during immersion), which was very similar to the case of the pure epoxy coating. The absence of L-CAR deprived the coating of self-healing functions. It should be noted that IACs-Ⅰ performs better on self-healing tests than IACs-Ⅱ, which can be analyzed from structures of the smart
35 nanocontainers. Compared with HMZSs-*d*150, L-CAR loaded HMZSs-*d*300 incorporated in IACs-Ⅰ have higher loading capacity and faster release rate under either acidic or alkaline environment, which are the important influential factors for self-healing coatings. Unlike the common sustainable release for
40 targeted drug delivery systems, the ideal status for self-healing is that high concentration of corrosion inhibitor molecules are compacted into the defected area within the shortest time, this state will promote efficiency of the spontaneous adsorption

process and form dense molecular film against corrosion. This is
45 the reason for the best self-healing performance of IACs-Ⅰ.

Conclusion

In the present study, the sol-gel protection method was used to synthesize HMZSs and avoid breakage of mesoporous zirconia shells during high-temperature calcination process. The HMZSs
50 were then used as scaffolds and directly bound with L-CAR to construct the smart nanocontainers as active components for IACs. Taking advantage of pH-dependent electrostatic interactions between HMZSs and L-CAR, the smart nanocontainers, L-CAR loaded HMZSs exhibit acid/alkaline-
55 responsive controlled release property, which facilitates them respond to pH variation occurring on corrosive micro-anodic and micro-cathodic zones and subsequently release mixed-typed corrosion inhibitor, L-CAR to stop anodic and cathodic activities. Importantly, the single loading-step simplifies the assembly
60 process of the smart nanocontainers and has the potential for large-scale production. The good compatibility between the smart nanocontainers and the components of water-borne epoxy coatings make L-CAR loaded HMZSs work normally. The uniformly distributed smart nanocontainers improve the
65 anticorrosion performance and play the crucial role in performing self-healing functions.

Experimental Section

Materials

Tetraethyl orthosilicate (TEOS, 99%), polyoxyethylene lauryl
70 ether (Brij 30, average Mn∼362), zirconium (Ⅳ) butoxide (80 wt% in 1-butanol), L-Carnosine (L-CAR, 98%) and polyvinylpyrrolidone (PVP, average Mn ∼ 40000) were purchased from Sigma-Aldrich. Araldite PZ 3961 and Aradur 3985 were purchased from Nanjing Golden Chemical Ltd., China.
75 All the other materials were analytical grade and used as received without any further purification. Water was purified with a Millipore Q system and had an electrical resistance of 18 MΩ·cm.

Preparation of HMZSs

A mixture of 10 mL (*20 mL*) H2O, 3.15 mL (*2 mL*) concentrated
80 ammonia and 75 mL ethanol was vigorously stirred for 30 min. After that, 6 mL (*3 mL*) TEOS was added to the mixture and then stirred for another 8 h. The monodispersed silica particles (*s*SiO$_2$) were obtained and dispersed in 200 mL ethanol containing 0.25 mL (*0.42 mL*) Brij 30 and 0.25 mL (*0.42 mL*) H$_2$O and the
85 mixture was stirred for 1 h. 1.5 mL (*2.5 mL*) zirconium butoxide was added dropwise to the mixture. After stirring for 12 h, the as-synthesized solid (*s*SiO$_2$@*s*ZrO$_2$) was collected by centrifugation, washed with water, and dispersed in 40 mL water. The solid was aged in water at room temperature for 1 day and dispersed in 100
90 mL water. 0.1 g PVP was added to modify the surface of zirconia, then the liquid phase was exchanged with ethanol by centrifugation and the collected solid was re-dispersed in 75 mL ethanol with 10 mL (*20 mL*) H$_2$O and 3.15 mL (*2 mL*) concentrated ammonia. After the addition of 6 mL (*3 mL*) TEOS,
95 the mixture was stirred for 8 h to form *s*SiO$_2$@*s*ZrO$_2$@*s*SiO$_2$. The solids were collected by centrifugation, washed thoroughly with water and ethanol, and calcined. The calcination step conducted under air with a heating rate of 2 K/min to 900 ℃. Finally, the product (*s*SiO$_2$@*m*ZrO$_2$@*s*SiO$_2$) was treated with NaOH (5 M) to
100 remove silica. The obtained HMZSs-*d*300 (HMZSs-*d*150) were washed with abundant water and ethanol, and dried under vacuum for further use. The inner diameter and shell thickness

were easily controlled by using different amount of corresponding chemical agents. According to the accurate dosages in the brackets as italic format, HMZSs-*d*150 can be prepared smoothly.

L-CAR Loading and Releasing Experiments

The loading of L-CAR was achieved via diffusion effect. The prepared HMZSs-*d*300 or HMZSs-*d*150 (40 mg) and L-CAR (250 mg) were dispersed into water (5 mL) with the aid of ultrasonication, and then stirred gently for 3 days to reach adsorption equilibrium at room temperature. The L-CAR loaded HMZSs-*d*300 or L-CAR loaded HMZSs-*d*150 were collected by centrifugation, rinsed with water (5 ml) once to remove the physisorption of L-CAR, and dried at 40 ℃ under vacuum overnight. To investigate the acid/alkaline-responsive release profiles, the L-CAR loaded HMZSs-*d*300 or L-CAR loaded HMZSs-*d*150 (1 mg) sealed in the dialysis bag were soaked in 3.8 mL solution at different pH value (neutral, PBS buffer solution 7.0; acidic, adjusted by HCl solution; alkaline, adjusted by NaOH solution). Finally, the real-time release of L-CAR in supernatant was recorded at one second interval by the UV/vis spectroscopy with the emission maximum at 210 nm over the entire period of release experiments.

Characterizations

The morphologies of HMZSs and the coatings were studied using a JEOL JSM-6390LV scanning electron microscope (SEM) coupled with energy dispersive X-ray (EDX) spectroscopy detector. Transmission electron microscopy (TEM) images, high resolution TEM (HRTEM) images and selected-area electron diffraction (SAED) patterns were obtained by a JEOL 2010 TEM operating at 200 kV. TEM samples were prepared by placing one drop of tested solid on copper grids covered with carbon. The wide-angle XRD data were recorded on a Bruker D8 Advanced diffractometer using Cu Kα radiation (λ=1.5405 Å). N2 adsorption-desorption isotherm was obtained at 77K on a Quanta Chrome Nova 1000 Micrometric apparatus. The specific surface area was calculated by the Brunauer-Emmett-Teller (BET) method. The pore size distribution was determined from the adsorption branch of the isotherm by the Barrett-Joyner-Halenda (BJH) method. Zeta-potential measurement was performed using a NonaBrook ZetaPALS. AFM (Vecco Brook DI) was used to characterize the topography of surface of coated carbon steel specimens and operated in tapping mode. The pH of solution was measured with a Mettler FE20-FiveEasy Plus pH meter. UV/vis spectroscopy was carried out with a Shimadzu UV-1800 spectrometer.

Fabrication and Anticorrosion Performance Evaluation of Intelligent Anticorrosion Coatings (IACs)

Carbon steel specimens (model: AISI 12L14) with dimensions of 4.0 cm × 2.0 cm × 0.2 cm were used as substrates. All the specimens were abraded using emery paper #400, washed by ultrasonication for 5 min in acetone followed by a water bath and finally dried in open air for further application. IACs-Ⅰ was prepared by dispersing of the L-CAR loaded HMSZs-*d*300 (0.52 g) into commercial epoxy resin, Araldite PZ 3961 (20.72 g) at room temperature, and followed by mixing coordinated hardner, Aradur 3985 (8.04 g) and small amount of H$_2$O (5.42 g). After stirred for 2 min, the mixture was coated on carbon steel specimen by spin-coating technique. Excess mixture was applied by injecting through a 0.2 μm syringe. The substrate was firstly rotated at a speed of 500 rpm for 1 min and then accelerated at 1000 rpm for another 1 min to create a uniform coating on

surface. The coated substrate was dried in air at 120 ℃ in a pre-heated oven for 2 h. As for IACs-Ⅱ, the whole procedure is similar to IACs-Ⅰ except for using the same amount of L-CAR loaded HMSZs-*d*150 instead of L-CAR loaded HMZSs-*d*300. The pure epoxy coating was fabricated without adding any smart nanocontainers. Electrochemical measurements were carried out using a PARSTAT 2273 Potentiostat/Galvanosat (Princeton Applied Research, USA) in a conventional three-electrode cell (open to air) containing working electrodes (carbon steel specimens or coated specimens), a platinum sheet as counter electrode and saturated calomel electrode (SCE) as reference electrode at 25 ℃. A Luggin-capillary was also included in the design, the tip of which was made very close to the surface of the electrode to minimize IR drop. Working electrodes were first immersed into the tested solution for 30 min to stabilize open circuit potential (OCP). Polarization plots were obtained at a scan rate of 0.166 mV s^{-1} in the potential range from -250 to +250 mV relative to OCP. The corrosion current densities were obtained from the intercept of extrapolated linear cathodic and anodic Tafel segments at the OCP. Electrochemical impedance spectroscopy (EIS) measurements were performed using AC signal with an amplitude perturbation of 10 mV at OCP in the frequency range 100 kHz to 10 mHz. The impedance data were fitted to appropriate equivalent circuits by using ZsimpWin software. Each electrochemical test was repeated three times under the same conditions, and very good repeatability was achieved. All potentials were measured against SCE. In order to slow down the corrosion rate and monitor self-healing phenomena occurring on artificial scratches, the SVET measurements were performed in 0.02 M NaCl solution using a M370 Scanning Electrochemical Workstation (Ametek, USA). Coated carbon steel specimens were glued to an epoxy holder only to leave 1.0 × 1.0 cm^2 surface area exposed to solution. The Pt-blackened electrode tip had a diameter of 20 μm and vibrated with 30 μm amplitude at the distance of 100 μm above the surface of coatings. The selected areas of 4.0 × 4.0 mm^2 were scanned and the local ionic current densities were mapped on a 21×21 grid, generating 441 data points. All the measurements were taken at OCP.

Acknowledge

Notes and references

^{a} School of Chemical Engineering, Nanjing University of Science and Technology, Nanjing, 210094, China. Fax: 86 025 84315609; Tel: 86 025 84315609; E-mail: fujiajun668@gmail.com

† Electronic Supplementary Information (ESI) available: [TEM images of broken HMZSs under different calcination temperature, Schematic representation of sol-gel protection method, XRD and N$_2$ adsorption-desorption isotherm and pore size distribution of HMZSs-*d*150, Zeta potential of HMZSs-*d*300, SEM images of HMZSs-*d*300, equilibrium adsorption configurations, optimized Structures, HOMO and LUMO of L-CAR and L-histidine, Tafel polarization curves of L-CAR, the dissociation equation of L-CAR and theoretical calculations for adsorption capacity and the SVET/EIS performances of IACs incorporated into unloaded HMZSs]. See DOI: 10.1039/b000000x/

1. A. E. Hughes, I. S. Cole, T. H. Muster and R. J. Varley, *NPG Asia Mater.*, 2010, **2**, 143.

2. X. D. Yu, L. M. Chen, M. M. Zhang and T. Yi, *Chem. Soc. Rev.*, 2014, **43**, 5346.
3. V. Amendola and M. Meneghetti, *Nanoscale*, 2009, **1**, 74.
4. D. Shchukin and H. Mohwald, *Science*, 2013, **341**, 1458.
5. D. Fix, D. V. Andreeva, Y. M. Lvov, D. G. Shchukin and H. Mohwald, *Adv. Funct. Mater.*, 2009, **19**, 1720.
6. G. O. Wilson, J. S. Moore, S. R. White, N. R. Sottos and H. M. Andersson, *Adv. Funct. Mater.*, 2008, **18**, 44.
7. M. X. Huang and J. L. Yang, *J. Mater. Chem.*, 2011, **21**, 11123.
8. L. P. Lv, Y. Zhao, N. Vilbrandt, M. Gallei, A. Vimalanandan, M. Rohwerder, K. Landfester and D. Crespy, *J. Am. Chem. Soc.*, 2013, **135**, 14198.
9. J. J. Wilker, *Nat. Mater.*, 2014, **13**, 849.
10. E. V. Skorb and H. Mohwald, *Adv. Mater.*, 2013, **25**, 5029.
11. S. R.White, N. R. Sottos, P. H. Geubelle, J. S. Moore, M. R. Kessler, S. R. Sriram, E. N. Brown and S. Viswanathan, *Nature*, 2001, **409**, 794.
12. K. S. Toohey, N. R. Sottos, J. A. Lewis, J. S. Moore and S. R. White *Nat. Mater.*, 2007, **6**, 581.
13. M. D. Hager, P. Greil, C. Leyens, S. van der Zwaag and U. S. Schubert, *Adv. Mater.*, 2010, **22**, 47.
14. M. Serdechnova, S. Kallip, M. G. S. Ferreira and M. L. Zheludkevich, *Electrochem. Commun.*, 2014, **41**, 51.
15. J. Tedim, S. K. Poznyak, A. Kuznetsova, D. Raps, T. Hack, M. L. Zheludkevich and M. G. S. Ferreira, *ACS Appl. Mater. Inter.*, 2010, **2**, 1528.
16. M. L. Zheludkevich, K. A. Yasakau, A. C. Bastos, O. Karavai and M. G. S. Ferreira, *Electrochem. Commun.*, 2007, **9**, 2622.
17. D. G. Shchukin, S. V. Lamaka, K. A. Yasakau, M. L. Zheludkevich, M. G. S Ferreira and H. Mohwald, *J. Phys. Chem. C*, 2008, **112**, 958.
18. G. L. Li, M. Schenderlein, Y. J. Men, H. Mohwald and D. G. Shchukin, *Adv. Mater. Interfaces.*, 2014, **1**, 1300019.
19. M. F. Hasse, D. O. Grigoriev, H. Mohwald and D. G. Shchukin, *Adv. Mater.*, 2012, **24**, 2429.
20. E. V. Skorb, D. Fix, D. V. Andreeva, H. Mohwald and D. G. Shchukin, *Adv. Funct. Mater.*, 2009, **19**, 2373.
21. A. Vimalanandan, L. P. Lv, T. H. Tran, K. Landfester, D. Crespy and M. Rohwerder, *Adv. Mater.*, 2013, **25**, 6980.
22. D. G. Shchukin, *Polym. Chem.*, 2013, **4**, 4871.
23. D. G. Shchukin and H. Mohwald, *Small*, 2007, **3**, 926.
24. M. L. Zheludkevich, J. Tedim and M. G. S. Ferreira, *Electrochim. Acta*, 2012, **82**, 314.
25. E. V. Skorb and D. V. Andreeva, *Polym. Chem.*, 2013, **4**, 4824.
26. J. J. Fu, T. Chen, M. D. Wang, N. W. Yang, S. N. Li, Y. Wang and X. D. Liu, *ACS Nano*, 2013, **7**, 11397.
27. T. Chen and J. J. Fu, *Nanotechnology*, 2012, **23**, 505705.
28. G. L. Li, Z. L. Zheng, H. Mohwald and D. G. Shchukin, *ACS Nano*, 2013, **7**, 2470.
29. Z. L. Zheng, X. Huang, M. Schenderlein, D. Borisova, R. Cao, H. Mohwald and D. Shchukin, *Adv. Funct. Mater.*, 2013, **23**, 3307.
30. E. Abdullayev and Y. Lvov, *J. Mater. Chem.*, 2010, **20**, 6681.
31. M. J. Hollamby, D. Fix, I. Donch, D. Borisova, H. Mohwald and D. Shchukin, *Adv. Mater.*, 2011, **23**, 1361.
32. D. Borisova, H. Mohwald and D. G. Shchukin, *ACS Nano*, 2011, **5**, 1939.
33. S. H. Tang, X. Q. Huang, X. L. Chen and N. F. Zheng, *Adv. Funct. Mater.*, 2010, **20**, 2442.
34. M. Taryba, S. V. Lamaka, D. Snihirova, M. G. S. Ferreira, M. F. Montemor, W. K. Wijting, R. Toews and G. Grundmeier, *Electrochim. Acta*, 2011, **56**, 4475.
35. P. M. Arnal, C. Weidenthaler and F. Schuth, *Chem. Mater.*, 2006, **18**, 2733.
36. B. Joo, Q. Zhang, I. Lee, M. DahI, F. Zaera and Y. D. Yin, *Adv. Funct. Mater.*, 2012, **22**, 166.
37. M. Bobina, A. Kellenberger, J. P. Millet, C. Muntean and N. Vaszilcsin, *Corros. Sci.*, 2013, **69**, 389.
38. M. A. Amin, K. F. Khaled, Q. Mohsen and H. A. Arida, *Corros. Sci.* 2010, **52**, 1684.
39. G. Vistoli, V. Straniero, A. Pedretti, L. Fumagalli, C. Bolchi, M. Pallavicini, E. Valoti and B. Testa, *Chirality*, 2012, **24**, 566.
40. S. V. Lamaka, M. Taryba, M. F. Montemor, H. S. Lsaacs and M. G. S. Ferreira, *Electrochem. Commun.*, 2011, **13**, 20.
41. M. F. Montemor, D. V. Snihirova, M. G. Taryba, S. V. Lamaka, I. A. Kartsonakis, A. C. Balaskas, G. Kordas, J. Tedim, A. Kuznetsova, M. L. Zheludkevich and M. G. S. Ferreira, *Electrochim. Acta*, 2012, **60**, 31.
42. D. G. Shchukin and H. Mohwald, *Adv. Funct. Mater.* 2007, **17**, 1451.
43. D. Borisova, D. Akcakayiran, M. Schenderlein, H. Mohwald and D. G. Shchukin, *Adv. Funct. Mater.*, 2013, **23**, 3799.

Journal of Materials Chemistry A Accepted Manuscript